Optik - International Journal for Light and Electron Optics 254 (2022) 168637

Contents lists available at ScienceDirect

Optik

journal homepage: www.elsevier.com/locate/ijleo

Analytical analysis and experimental validation of optical power estimation in V-grooved polymer optical fibers

Şekip Esat Hayber

Department of Electrical-Electronic Engineering, Kırşehir Ahi Evran University, Kırşehir 40100, Turkey

ARTICLE INFO

Keywords:
Polymer/plastic optical fiber
Geometrical optics
V-grooved POF
Optical power

ABSTRACT

In this study, analytical and experimental research of V-grooved polymer optical fibers (POFs)' optical power loss characteristics is carried out. A simple mathematical model that can determine the optical output power and loss in the V-grooved structure depending on the groove angle and depth has been developed using geometric optic approaches. This model is used to analyze the effects of groove parameters and fiber diameter on optical output power in detail. Then, a low-cost and efficient groove fabrication process is performed, and V-grooves with 45° half-angle and 200 μm groove depth are created on POFs with diameters of 1 mm, 2 mm, and 3 mm to be used in the experiment. When the effect of groove numbers ranging from 5 to 25 on the optical output power is examined, the behavior obtained from the experimental results is compatible with the analytical results. Output power can be estimated with greater than 95% accuracy for V-groove POF structures, optimizing the ratio of groove depth to fiber core radius for a specific groove angle.

1. Introduction

Nowadays, plastic or polymer optical fibers (POFs) are of great interest because they have both the simplicity of copper cables and the speed characteristics of silica fibers. Although most optical fibers are made of doped silica glass, POFs are becoming widespread in different fields thanks to these superior properties. Due to its advantages such as POFs have large alignment tolerances, can be terminated with inexpensive connectors, are lighter, allow operation in the visible spectrum, are more flexible due to bending, shock, and vibration resistance, immunity to electromagnetic interference, use of low-cost and straightforward test equipment, require cheaper light-emitting diode sources and photodetectors, it is attracting the attention of researchers and the industry [1]. Moreover, with minimal training and elementary tools, an amateur can quickly terminate a POF in a couple of minutes. However, POFs have disadvantages such as high losses at long distances, limited systems and suppliers, lack of knowledge in installation and design, and limited research and development studies [1,2]. Despite all these disadvantages, POFs are increasingly important in applications that do not require long transmission distances, such as biomedical, automotive, aircraft control systems, and consumer electronics [3]. Besides short distance communication applications, POFs are used in decorative and lighting for road signs, museums where the feature of not transmitting ultraviolet radiation is handy, widely used in image transmission, and endoscopes and sensing applications [4].

One of the most important application areas of POFs is sensors, and most sensing assemblies produced with POFs made of different polymers are based on simple and convenient intensity-based systems [5]. In the literature, physical and chemical parameters can be

E-mail address: sehayber@ahievran.edu.tr.

https://doi.org/10.1016/j.ijleo.2022.168637
Received 25 November 2021; Received in revised form 16 January 2022; Accepted 20 January 2022
Available online 22 January 2022

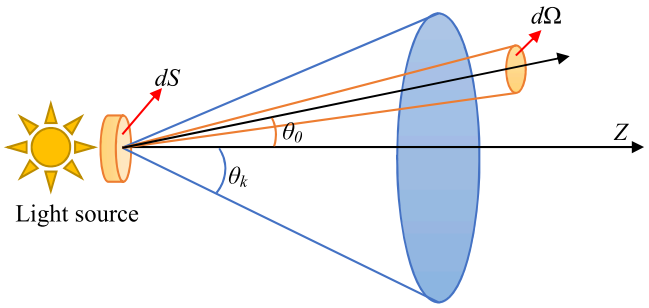

Fig. 1. Elemental source area dS emits light into solid angle $d\Omega$ within a cone of half-angle θ_k.

detected such as liquid level [6,7], vibration [8,9], gas monitoring [10], sugar content [11], milk fat [12,13], refractive index [14], curvature [15], strain [16], and nucleic acid [17]. All these sensor groups can be classified into four groups as bulk scattering, bending, surface plasmon resonance, and surface structural modification [1,18]. In the first bulk scattering, by adding nanomaterials to POFs, certain absorption and scattering centers are created in the structure. The second, bending, is based on the principle that the light interacts with the environment as side-emitting by bending the fiber in certain proportions and shapes. In the third, surface plasmon resonance creates an evanescent field on the surface by coating different metallic materials on the fiber core. Finally, surface structural modification; is based on the principle that the light is side-emitting from these regions by creating perforations on the fiber surface and interacting with the environment [19]. Among these four, the surface structural modifications technique draws attention because it is easy and low-cost.

Surface structural modifications, which cause light leakage from the fiber surface by preventing the total internal reflection (TIR) in the fiber, can be formed in a controlled manner with a smooth geometry or in a random way [18]. Fabrication processes are based on abrasive material removal, chemical, and thermal surface structural modifications. Researchers have performed different types of side-emitting processes by forming rectangular [20], curved [21], V-shaped [22] grooves on the fiber surfaces. Although the geometry based on the V-groove shape was introduced in the early seventies [23], it was used in a curvature sensor application by Djordjevich and Boskovic in 1996 [24]. Djordjevich et al. used the curvature sensor they developed in the following years experimentally in deflection [25,26], strain [27] measurements. The first analytical study was carried out by Kovacevic et al. in 2008, in a study group that Djordjevich was also in [22]. This analytical equation for curvature detection, which is not precisely resolved, was used experimentally by Fu et al. in their light intensity modulation-based study for curvature detection [28,29]. Similar studies continued by Di et al. [15,30] and Zhi and Di turned the curvature sensor into a mechanism for detecting wind speed in their recent study [31]. Shen turned V-groove structures into wearable form-fit fiber fabrics for phototherapy applications [32,33]. In the following years, Wei Zheng continued similar wearable applications for human respiration monitoring [16]. In this way, different wearable applications based on the same basic principle continue up to date [34–36]. Teng et al. have performed displacement sensing using the easy fabrication and low-cost features of the V-groove structure [37]. In all of these studies, the curvature gauge feature of the first appearance of the V-groove structure is used.

Straight applications of the V-groove structure were used by André et al. to monitor the concrete curing process [38]. The study tried to determine the cement setting ratio during the curing period by monitoring the intensity of the light signal received from the output of the V-groove structure over time. The liquid level measurement in oil piping or fuel tanks was carried out experimentally by Antunes et al. [39]. Mesquita et al. used a similar structure for monitoring groundwater levels [40]. Similar studies, which are based on the principle of increasing the optical intensity at the output by re-guiding the light beam leaking from the fluid-filled between the grooves to the fiber, continue until today [41–44]. The common feature of the studies is intensity-modulated experimental applications based on the principle of correlating the changing optical power at the output of the straight multiple V-grooved structures with the liquid level or the refractive index of the liquid. However, the lack of a mathematical model for the determination of the power to reach the output according to the groove geometry and number of the straight multiple V-groove structures in the literature limits the diversity and potential of these applications.

In this study, an analytical model is derived for determining the optical intensity at the output according to parameters of V-grooves on a straight POF. Thanks to this developed model, a detailed analysis of the power to reach the output according to the groove depth, groove angle, and a groove number have been made for fibers of different diameters. Grooves of specific geometric sizes and numbers were fabricated on POFs with 1 mm, 2 mm, and 3 mm diameters. The optical power at the output was measured to validate the model. The obtained experimental results were compared with the analytical model, and the compatibility of the results with each other and the model's accuracy was proved. This developed model will allow researchers to associate the power to reach the output with the parameter to be measured in sensor designs.

2. Model development

2.1. Theory

A light source can be defined by the amount of power in a conical shape spreading out from the differential dS element belonging to

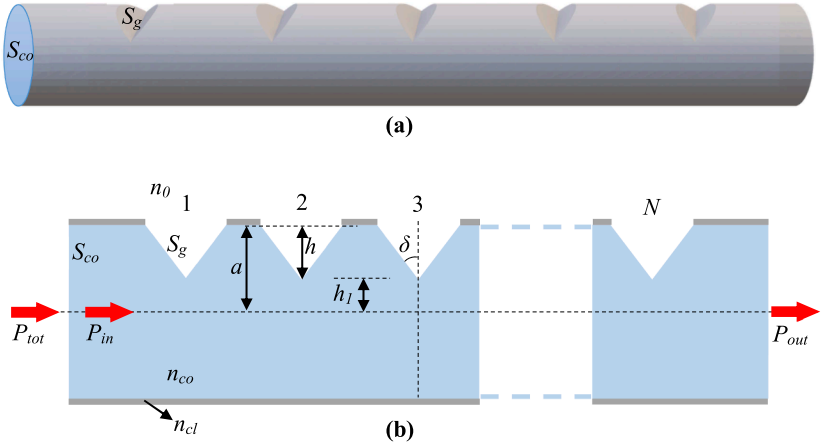

Fig. 2. Geometry of V-grooved POF, **(a)** 3D, **(b)** cross-section view.

its surface. In Fig. 1, the differential dS element θ_k propagates in a half-angle cone. The light emitted in the $d\Omega$ area at an angle of θ_0 with the normal to the source surface has a density $I(\theta_0)$ emitted per unit area of the source. Thus, the radiated power is given by Eq. (1) [45].

$$dP = \begin{cases} I(\theta_0)dSd\Omega, & 0 \le \theta_0 \le \theta_k \\ 0, & \theta_k \le \theta_0 \le \pi/2 \end{cases} \tag{1}$$

Where $d\Omega$ shown in Fig. 1 is the element of the solid angle.

The diffuse or Lambert source term benefits when each differential area dS of the source emits light in all directions. This is the most common source in practice and approaches the output of light-emitting diodes. The density distribution of $\theta_k = \pi/2$ Lambertian sources is given by Eq. (2) with I_0 constant [22,45].

$$I(\theta_0) = I_0 \cos\theta_0, \quad 0 \le \theta_0 \le \pi/2 \tag{2}$$

(r, φ) are polar coordinates relative to the fiber axis and $(\theta_0, \theta_\varphi)$ are spherical polar angles concerning the incidence normal vector to indicate the area, dS, and solid angle, $d\Omega$, are given in Eq. (3) and Eq. (4), respectively.

$$dS = rdrd\varphi \tag{3}$$

$$d\Omega = \sin\theta_0 d\theta_0 d\theta_\varphi \tag{4}$$

where the range of source-ray directions satisfies $0 \le \theta_0 \le \pi/2$, $0 \le \theta_\varphi \le 2\pi$, and the range of positions on the end face satisfies $0 \le r \le R$, $0 \le \varphi \le 2\pi$. The dP power element radiating from the dS area at a solid angle of $d\Omega$ takes the following form.

$$dP = I_0 \cos\theta_0 rdrd\varphi \sin\theta_0 d\theta_0 d\theta_\varphi \tag{5}$$

By integrating Eq. (5), the total power radiated by the source in all directions, P_{tot} can be calculated over the full range of values for each of the four variables given above.

$$P_{tot} = \int_0^R rdr \int_0^{2\pi} d\varphi \int_0^{2\pi} d\theta_\varphi \int_0^{\pi/2} I_0 \cos\theta_0 \sin\theta_0 d\theta_0 \tag{6}$$

Here the illumination is uniform and P_{tot} can also be given as in Eq. (7).

$$P_{tot} = \pi^2 R^2 I_0 \tag{7}$$

Along the cross-sectional area (S_{co}) of fiber with radius, a, and acceptance angle θ_a shown in Fig. 2, the total luminous power, P_{in}, is obtained by integrating the dP given in Eq. (5). The P_{in} is the amount of power corresponding to the cross-sectional area, S_{co} of the fiber. Therefore, in integration, the upper limit of r is a, and the upper limit of θ_0 is θ_a.

$$P_{in} = \int_0^a rdr \int_0^{2\pi} d\varphi \int_0^{2\pi} d\theta_\varphi \int_0^{\theta_a} I_0 \cos\theta_0 \sin\theta_0 d\theta_0 \tag{8}$$

Eq. (8) can also be expressed as [2],

$$P_{in} = \int_{-a}^{a} 2\sqrt{(a^2 - h_1^2)}dh_1 \int_0^{2\pi} d\theta_\varphi \int_0^{\theta_a} I_0 \cos\theta_0 \sin\theta_0 d\theta_0 \tag{9}$$

Where h_1 represents the outward radial distance from the fiber core axis, as seen in Fig. 2(b), the same expression in Eq. (10) is obtained from the solution of both equations.

$$P_{in} = \pi^2 a^2 I_0 \sin^2\theta_a \tag{10}$$

Here the acceptance angle, θ_a, is given as,

$$\sin\theta_a = \frac{\left(n_{co}^2 - n_{cl}^2\right)^{1/2}}{n_0} \tag{11}$$

Where n_{co}, n_{cl}, and n_0 represent the refractive indices of the fiber core, fiber cladding, and medium, respectively.

The optical power corresponding to the surface of the first groove, S_g of the structure in Fig. 2, is expressed as,

$$P_g = \int_{a-h}^{a} 2\cos\delta\sqrt{(a^2 - h_1^2)}dh_1 \int_0^{2\pi} d\theta_\varphi \int_0^{\theta_a} I_0 \cos\theta_0 \sin\theta_0 d\theta_0 \tag{12}$$

Where h and δ represent groove depth and groove half-angle, respectively. Eq. (13) is derived from the solution of Eq. (12). The optical power reached the groove can be calculated from Eq. (13).

$$P_g = \cos\delta\left[\left(\frac{a^2\pi}{2}\right) - (a-h)\sqrt{2ah - h^2} - a^2\sin^{-1}\left(\frac{a-h}{a}\right)\right]\pi I_0 \sin^2\theta_a \tag{13}$$

Thus, thanks to being able to calculate P_g, the proportion of power on surface S_g is found as,

$$\alpha = \frac{P_g}{P_{in}} = \frac{\cos\delta\left[\left(\frac{a^2\pi}{2}\right) - (a-h)\sqrt{2ah - h^2} - a^2\sin^{-1}\left(\frac{a-h}{a}\right)\right]\pi I_0 \sin^2\theta_a}{\pi^2 a^2 I_0 \sin^2\theta_a} \tag{14}$$

When this equation is simplified, we get a helpful equation that depends on the h/a ratio,

$$\alpha = \frac{\cos\delta}{\pi}\left[(\pi/2) - (1-h/a)\sqrt{2(h/a) - (h/a)^2} - \sin^{-1}(1-h/a)\right] \tag{15}$$

Provided that all the V-grooves are identical, the power ratios α in the other grooves will also be the same. Accordingly, the amount of power that can reach the output by passing all the grooves is defined as in P_{out} Eq. (16). The obtained equation is compatible with the literature [29]. Expressions in parentheses in Eq. (16) represent the relative loss values for a single groove. Therefore, the output power in a POF structure consisting of N grooves is obtained as follows.

$$P_{out} = P_{in}\left(1 - \frac{P_g}{P_{in}}\right)^N = P_{in}(1-\alpha)^N \tag{16}$$

In this case, the relative transmission loss, δP, can be calculated as follows,

$$\delta P = \frac{P_{in} - P_{out}}{P_{in}} \tag{17}$$

It is also possible to alternatively calculate the output power at the end of the groove structure. For a POF with identical multiple V-grooves as in Fig. 2, we can obtain the power loss for the first groove.

$$P_{g_1} = P_g \tag{18}$$

Since the power ratio in each groove to the power at the input will be the same due to the above assumptions, the powers in the second and third groove are given as follows.

$$P_{g_2} = \left(P_{in} - P_{g_1}\right)\frac{P_g}{P_{in}} = P_g\left(1 - \frac{P_g}{P_{in}}\right) \tag{19}$$

$$P_{g_3} = \left(P_{in} - P_{g_1} - P_{g_2}\right)\frac{P_g}{P_{in}} = P_g\left(1 - \frac{P_g}{P_{in}}\right)^2 \tag{20}$$

The same process is repeated for the remaining grooves, and the power in the Nth groove becomes as follows.

$$P_{g_N} = \left(P_{in} - P_{g_1} - P_{g_2} - P_{g_3} - \ldots - P_{g_{N-1}}\right)\frac{P_g}{P_{in}} = P_g\left(1 - \frac{P_g}{P_{in}}\right)^{N-1} \tag{21}$$

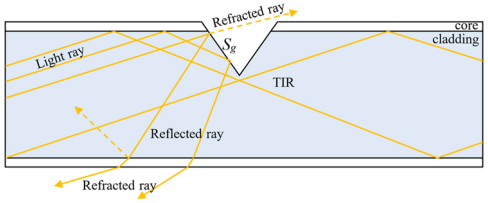

Fig. 3. Ray paths in V-grooved POF.

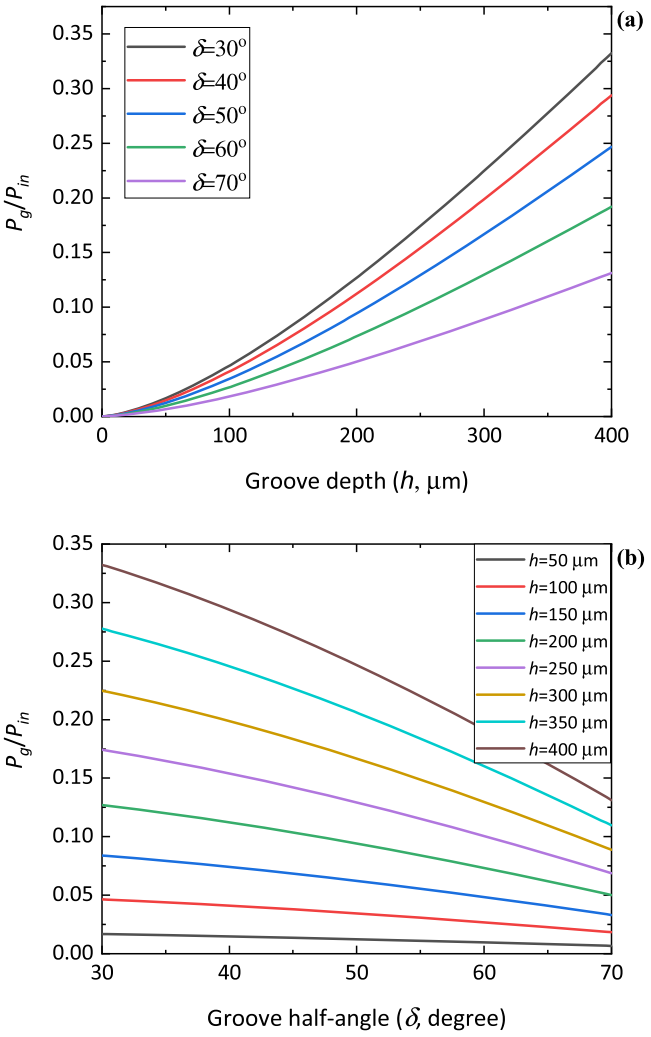

Fig. 4. Variation of the power ratio, P_g/P_{in} with **(a)** the groove depth for various groove half-angle, **(b)** the groove half-angle for various groove depth.

The sum of the optical powers in the N grooved system can be obtained.

$$P_{gtot} = \sum_{i=1}^{N} P_g \left(1 - \frac{P_g}{P_{in}}\right)^{i-1} = P_{in} - P_{in}\left(1 - \frac{P_g}{P_{in}}\right)^{N} \tag{22}$$

The difference between the input power of the fiber and the total power in the grooves is equal to the output power when fiber termination losses and other additional losses are neglected. Therefore, the term P_{out} can be re-written as Eq. (23).

$$P_{out} = P_{in} - P_{gtot} = P_{in}\left(1 - \frac{P_g}{P_{in}}\right)^{N} = P_{in}(1-\alpha)^{N} \tag{23}$$

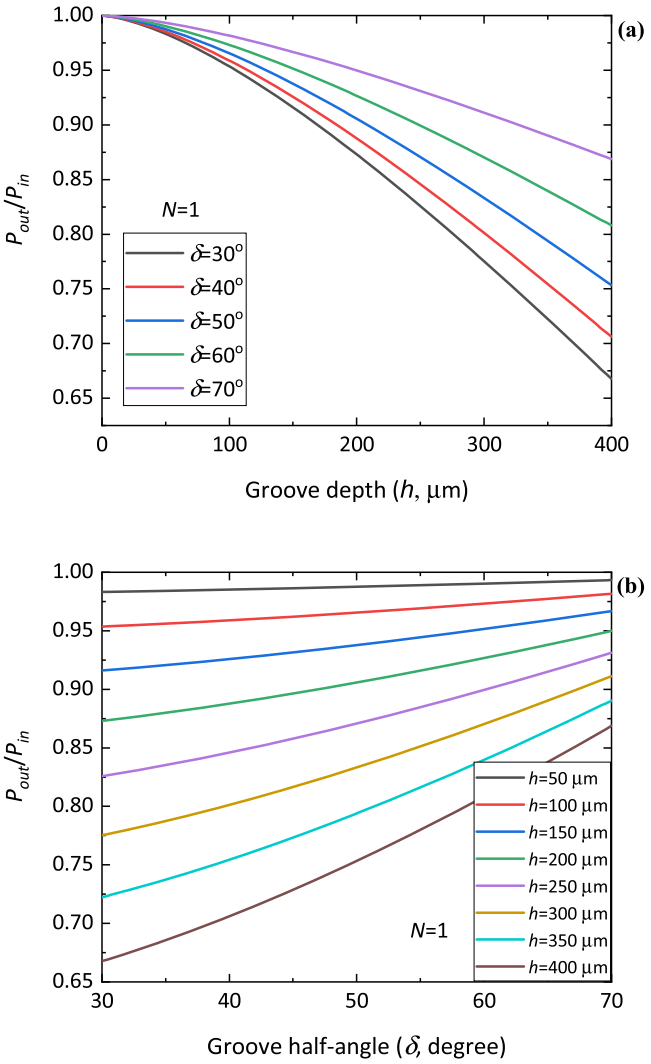

Fig. 5. Variation of the power ratio, P_{out}/P_{in} with (a) the groove depth for various groove half-angle, (b) the groove half-angle for various groove depth. (Groove number=1).

This equation agrees with Eq. (16) obtained above. This equation represents the power losses due to the grooves.

As seen in Fig. 3, the optical power on the surface of the V-groove contains the refracted and reflected power. Some of this reflected power will be refracted from the opposite interface [18], and some will return to the fiber input [32]. In other words, the light rays corresponding to the S_g surface represent the loss powers that cannot reach the output because they cannot satisfy the TIR condition [46]. The amount of reflected and refracted light depends on the groove geometry, the angle of incidence, and the refractive indices of both the fiber core and the medium in contact with the core.

2.2. Numerical results

We mentioned that for the V-grooved POF, since the optical power from each groove is now computable, the incident light from the groove will create a loss mechanism that will not reach the output. To better understand the behavior of the analytical solutions given by Eq. (15) according to the groove parameters, the calculations according to the groove depth and groove half angle for the single groove structure are shown as in Fig. 4. 1 mm diameter POF with a core radius of 490 mm was used in the calculations. Depending on the groove geometry, the optical power that will be lost can be optimized according to the application area. It is seen that the power loss increases as the groove depth increases, but the power loss decreases with the rise of the groove half-angle. As explained in Section 2.1, the incident light into the groove surface causes loss with different scenarios, making it difficult to measure this power.

In a POF, the optical power at the output is intentionally or unintentionally weakened due to different loss mechanisms. The transmission, coupling, etc., induced losses are negligible compared to V-groove losses, which are a good alternative for sensor applications. The typical attenuation is 150 dB/km @ 650 nm, and the attenuation is approximately 0.037 dB for a 25 cm section

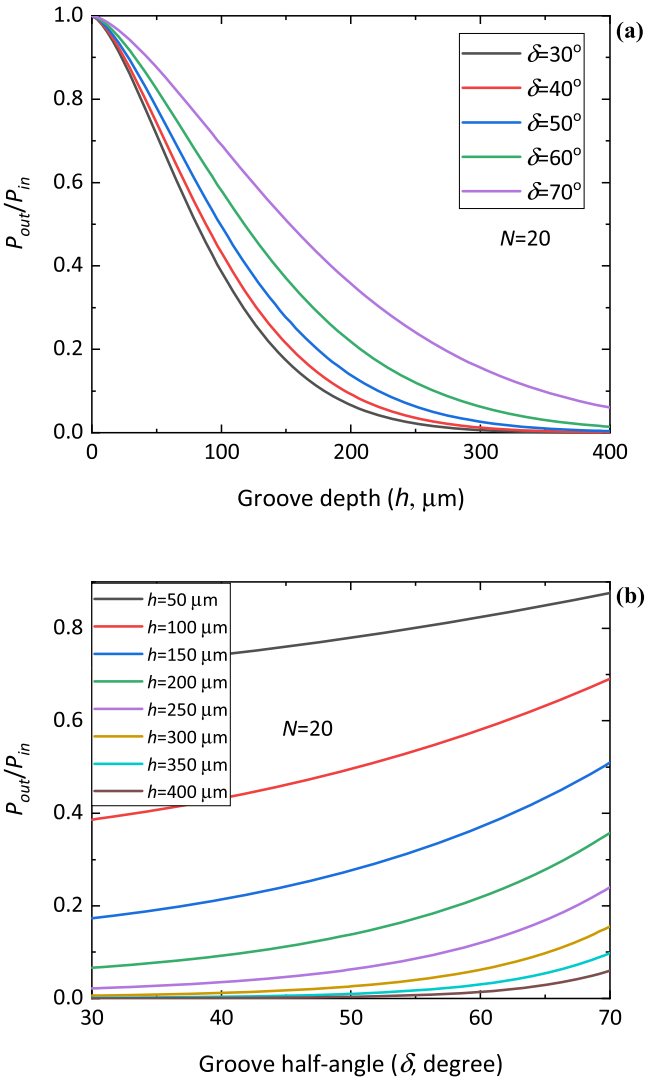

Fig. 6. Variation of the power ratio, P_{out}/P_{in} with (a) the groove depth for various groove half-angle, (b) the groove half-angle for various groove depth. (Groove number=20).

produced from POF. This attenuation does not cause a significant change in output power. Therefore, by calculating the power reaching a single groove, the optical power at the output of the groove structure can be estimated. Fig. 5 shows the variation of the optical output power according to the groove depth and groove half-angle. It is understood that increasing groove depth causes a decrease; groove angle has the opposite effect of groove depth on output power. It can be seen from Fig. 5(b) that the structure with low groove depths (e.g., 50 μm, 100 μm) does not significantly change the output power regardless of the groove angle.

Fig. 6 shows the effect of groove parameters on normalized output power in a POF structure with multiple identical grooves. The output power decreases sharply depending on the increasing groove depth of the structure consisting of 20 grooves. It is seen that the normalized optical output power is at the level of 3 dB depending on δ after a depth of about 150 μm. At small δ and higher h, the output power remains below 10% of the input (Fig. 6(b)).

Calculations performed at selected h and δ values to understand the change in output power according to the changing groove number are shown in Fig. 7. The effect of the groove number on the output power can be linear or a rapidly decreasing exponential curve in Fig. 7(a). While it exhibits a linear variation at low groove depths (e.g., 50 μm, 100 μm), it shows rapidly decreasing exponential behavior at significant depths (e.g., 400 μm, 350 μm, and 300 μm). In Fig. 7(b), when the h value is selected as 200 μm, the effect of the groove number on the output power at different δ can be seen. In grooves with $\delta = 30°$, there is a 3 dB attenuation at the output after 5 grooves. In addition, when $\delta = 70°$, the attenuation in output power becomes 3 dB after about 14 grooves.

After all these calculations, h= 200 μm and $\delta = 45°$ values were chosen for experimental measurements. Fig. 8 plotted for three different POF diameters with the help of the derived model. The decreasing trend of optical power at the output according to the diameter varies for each diameter. The output power reaches a 3 dB limit after 6 grooves, 17 grooves for 1 mm, 2 mm diameters,

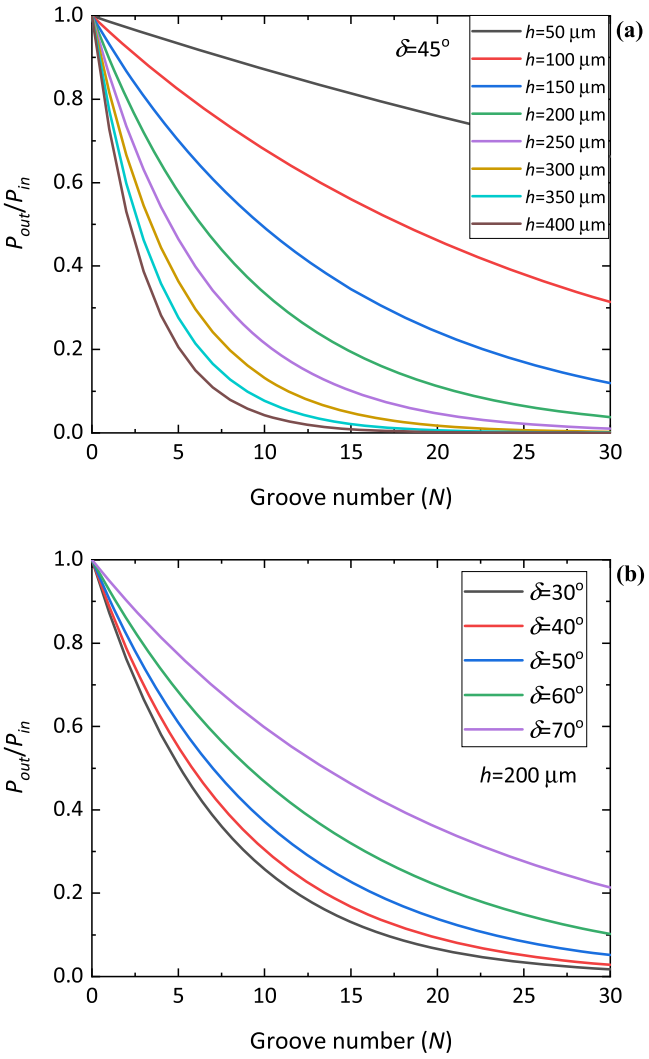

Fig. 7. Variation of the power ratio, P_{out}/P_{in} with the groove number (a) for various groove depths ($\delta = 45°$), (b) various groove half-angle (h=200 μm).

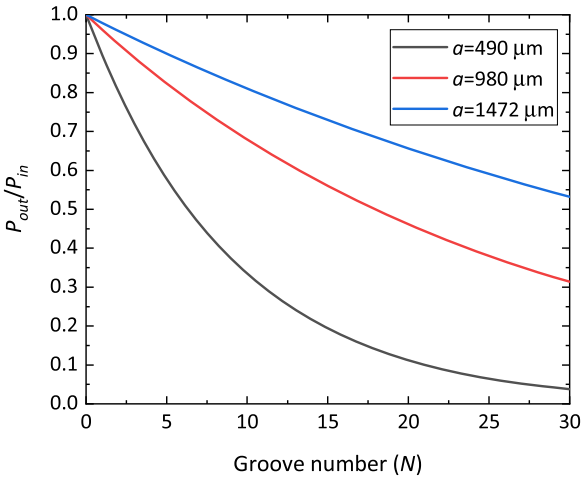

Fig. 8. Normalized optical power versus groove number.

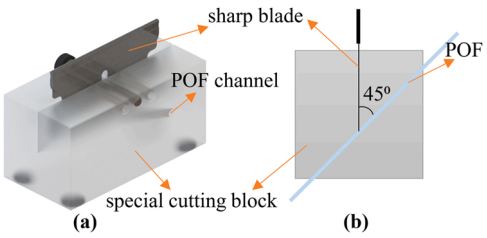

Fig. 9. (a) Special 45º cutter, (b) cross-section.

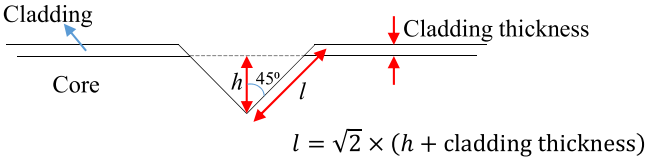

Fig. 10. Calculation of the cutting depth.

Table 1
POF probe parameters.

a (μm)	*h* (μm)	*l* (μm)	*δ* (°)	*N*
490	200	297	45	5, 10, 15, 20, 25
980	200	311	45	5, 10, 15, 20, 25
1472	200	322	45	5, 10, 15, 20, 25

respectively. The optical power decreases exponentially since 1 mm POF has the maximum perturbation.

Moreover, it is seen that the optical power loss does not reach the 3 dB limit for a 3 mm POF due to the groove depth effect. Keeping the groove depths constant while the diameter changes, the effect of the groove number on the output can change linearly or exponentially. The linear behavior at low groove depths agrees with the literature and is preferred in various applications such as liquid level and refractive index detection [39,41,44]. Furthermore, its ability to calculate the output power according to the groove number, half-angle, and depth allows researchers to optimize detection sensitivity and accuracy. In this respect, the developed model will be able to fulfill a gap in the literature.

3. Fabrication and experimental results

3.1. Fabrication process and experimental setup

Three different diameters of bare polymer fibers were used in the experimental study. The fiber cores are made of polymethyl methacrylate (PMMA), while the claddings are made of fluorinated polymer material. The part numbers of bare polymer fibers, which have features such as non-critical alignment of both light sources and fibers, good mechanical properties, low attenuation at the visible range of the lighting spectrum, are OMPF1000, OMPF2000, and OMPF3000. The OMPF1000, OMPF2000, and OMPF3000 have core/cladding diameters of 980/1000 μm, 1960/2000 μm, and 2944/3000 μm, respectively. These fibers, which have a numerical aperture of 0.5 and a core refractive index of 1.49, have a temperature range of − 55ºC to + 70ºC.

First of all, each fiber of three different diameters was cut vertically with a 25 cm long fiber optic side cutter (1PK-258A). The two ends of the fibers are polished by sanding with a polishing kit (Broadcom HFBR-4593Z) to minimize coupling losses. Then, to make a 45° cut on the POF, a total of 15 V-grooved fibers were created by adjusting the distance between the groove centers by 1 mm with the help of a special cutting block (FF-LCP-45DEG) (Fig. 9(a)). Thus, the length of the grooved section varies between 5 mm and 25 mm. POFs with diameters of 1 mm and 2 mm were easily cut with this tool, but the tool channel was extended to 3 mm for a 3 mm POF. It is a handy tool that lets cut an accurate 45° on POF fiber.

The depth h was desired to keep equal for all three fibers. Since the fiber claddings are of different thicknesses, the cutting depth, l of the blade must be different. Fig. 10 explains this situation. The calculation of the l values given in Table 1 was determined as $l_{1mm} = \sqrt{2} \times (200\mu m + 10\mu m) \cong 297\mu m$, $l_{2mm} = \sqrt{2} \times (200\mu m + 20\mu m) \cong 311\mu m$, $l_{3mm} = \sqrt{2} \times (200\mu m + 28\mu m) \cong 322\mu m$. Desired depth values were set manually by pushing the cutter blade towards the fiber and measuring the outside part of the blade with the help of a digital micrometer.

The grooves on the fiber surface and the light leaking from the grooves are seen in Fig. 11 (a). As seen in Fig. 11 (b), experiments were carried out using a laser source with a wavelength of 650 nm and an optical power meter. The optical power at the output was read from a reference probe without a groove and recorded as the normalization reference for three different diameter fibers. Three

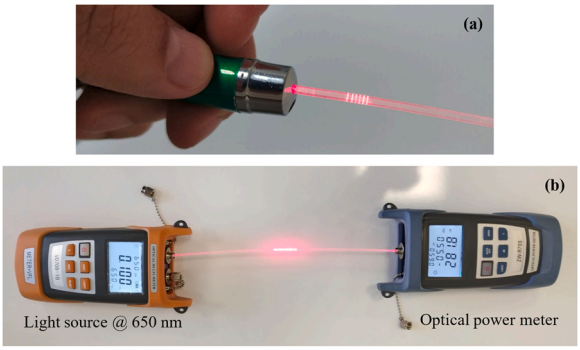

Fig. 11. **(a)** V-grooved POF structure, **(b)** experimental setup.

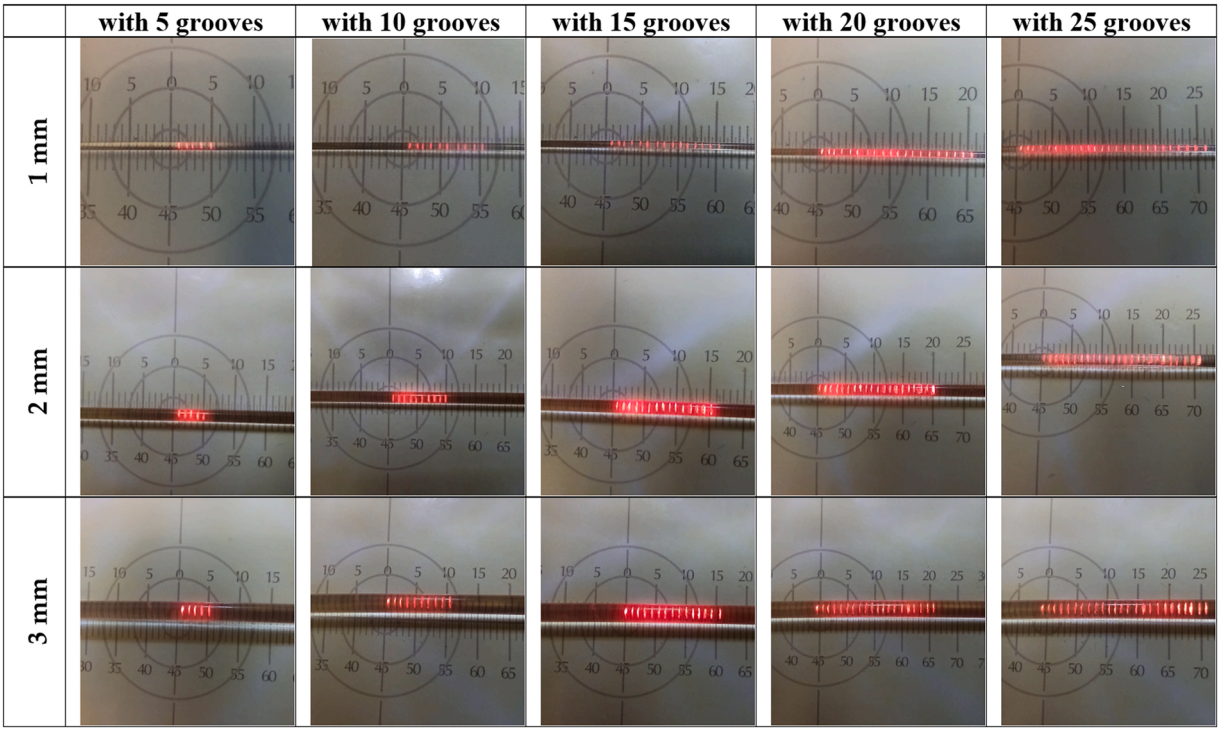

Fig. 12. Demonstration of V-grooved POF probe samples.

different fiber probes were prepared to minimize groove fabrication and measurement errors for each diameter. The data were obtained by taking the average of the measured optical power for each of them.

3.2. Experimental Results

According to the experimental procedure described in Section 3.1, the output value from the reference probe was recorded. The optical power was measured after groove numbers 5, 10, 15, 20, and 25 from the grooved on the 1 mm POF. This process was repeated on 3 POF probes of the same diameter, and the results were averaged. Similar procedures were repeated for the 2 mm and 3 mm POF probes. As seen in Fig. 12, some of the light reaching the groove is emitted from the groove surfaces, while some are refracted due to the light rays perpendicular to the surface opposite the grooves. Since the light losses here cannot be measured directly, the loss amounts can be calculated by measuring the optical power at the output.

As seen in Fig. 13, analytical and experimental results obtained from POF probes of 3 different diameters are given comparatively. Fig. 13 (a) shows a decrease in the normalized optical power due to the increasing groove numbers on the 1 mm diameter POF. The solid black line represents the analytical results, and the red dots represent the mean of three experimental data measured from 6 points ($N = 0$, 5, 10, 15, 20, and 25). Similarly, Fig. 13 (b) and (c) are for the other two POF types with the core radius of 980 μm and

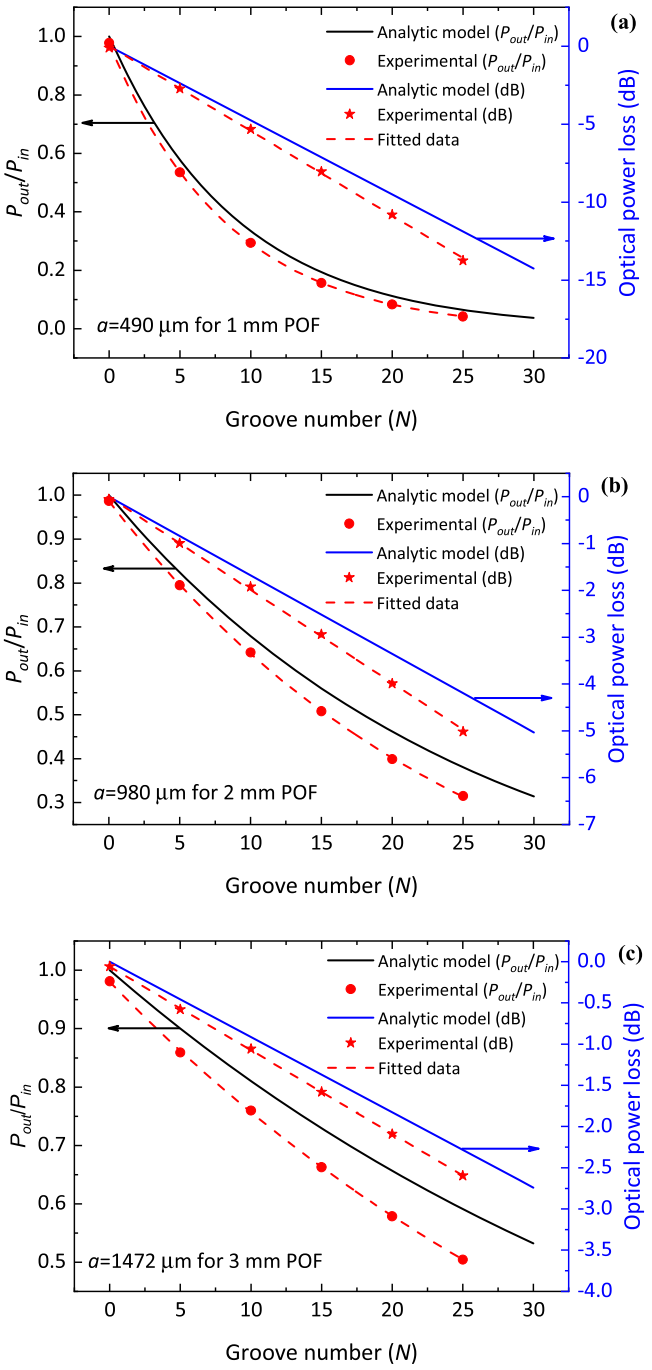

Fig. 13. Comparison of the analytical model and experimental results for (a) 1 mm, (b) 2 mm, and (c) 3 mm POFs.

1472 μm, respectively. The normalized optical power at the output is higher than the POF probe with a core radius of 490 μm. This phenomenon can be interpreted as the α value given by Eq. (15) increases with increasing h/a ratio and thus decreases the output power.

The average percent error value for the 1 mm diameter V-grooved POF structure with a ratio of h/a= 0.41 reached a high value of 19.92%. However, while this value is 9.83% in the 2 mm structure, it is 4.71% for the 3 mm structure. The h/a ratio is 0.20 and 0.14 for 2 mm and 3 mm POFs. From this point of view, the output power can be estimated with less than 5% error for V-grooved POF structures with an approximate h/a= 0.15 ratio. As the h/a ratio decreases, the rate of production errors gradually decreases.

Fig. 14 shows the variation of normalized output power according to the groove depth. In the experimental study, the output power is first measured and recorded from a 25 cm long POF sample with a= 980 μm value. Then, the h is increased from 50 μm (l≅99 μm) to

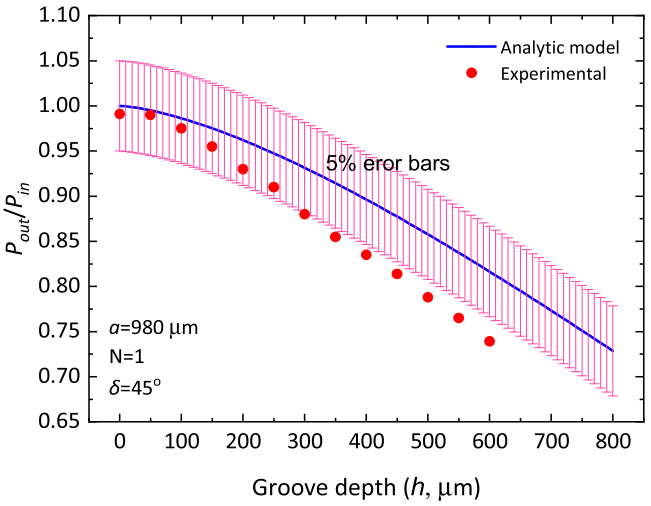

Fig. 14. Comparison of the analytical model and experimental results for the variation of power ratio with groove depth.

600 µm (l≦877 µm) with 50 µm step intervals. Output power is measured after each cut. 5% error bars are seen in Fig. 14. The average percent error of all measurements is about 5.3%. In cases where the depth of the groove is more significant than 250 µm, it is seen that the measurement error goes beyond the 5% range. It is seen that the error rate increases as the h/a ratio increases in parallel with the experimental test results according to the groove numbers.

Among the reasons why the experimental results are generally below the analytical results, the most significant factor is the errors in the production of the grooves. In addition, the effect of temperature and the stability of the light source are other factors that affect the measurements. However, these effects could be eliminated by normalizing the results obtained with the grooveless probes used during the experiments. In this study, the obtained results were normalized, so only fabrication irregularities remain among the errors that cause measurement errors. The model's accuracy has been demonstrated as a fundamental principle. These errors can be minimized as much as possible with advanced manufacturing techniques by micro-electro-mechanical systems/nano-electro-mechanical systems.

4. Conclusion

Standard POFs have a high numerical aperture allowing millions of propagated rays. Radiation losses in these fibers are usually calculated using a geometric optics approach. However, the exact solution of complex equations in these geometric approaches is not always possible. Similarly, in this study, a valuable and straightforward analytical model is derived by solving incompletely solved equations for straight V-grooved POFs. Thanks to this derived model, the groove induced power loss and the output power can be calculated according to all groove parameters. By changing the groove parameters, the optical power at the output was calculated for a 1 mm POF, and the V-grooved structures were optimized. It was observed that the optical power at the exit decreased with increasing groove depth. It increased with increasing groove angle. According to the number of grooves, the optical power variation at the output was examined when the grooves were identical. It was observed that optical power loss curves of V-groove structures could be linear or exponential when $\delta = 45°$ and h= 200 µm were selected. Optimized V-grooved structures were produced experimentally, and the results were compared by measuring the optical power at the output for grooves at specific intervals such as 5, 10, 15, 20, and 25. It was shown that the obtained experimental results converged to the analytically calculated curves and the model was correct. Researchers can calculate the optical power at the output for different sensor designs using this model.

Declaration of Competing Interest

The author declare that they have no known competing financial interests or personal relationships that could have appeared to influence the work reported in this paper.

References

[1] H. Pan, in: M.M. Werneck, R.C.D.S.B. Allil (Eds.), Introduction: Why Plastic Optical Fibers? In Plastic Optical Fiber Sensors, 1st ed.,, CRC Press, Boca Raton, FL, USA, 2019, pp. 1–20. ISBN 9781315098593.
[2] M.G. Kuzyk, Chapter 1: History of Polymer Optical Fibers. In Polymer Fiber Optics, CRC Press, Boca Raton, FL, USA, 2007, pp. 1–13. ISBN 15744470688.
[3] L. Bilro, N. Alberto, J.L. Pinto, R. Nogueira, Optical sensors based on plastic fibers, Sensors 12 (9) (2012) 12184–12207.
[4] K.S. Thyagarajan, A. Ghatak, Chapter 4: optical fibers. Fiber Optic Essentials, Wiley & Sons, Inc.,, Hoboken, New Jersey, 2007, pp. 28–54. ISBN 9780470097427.
[5] A.G. Leal-Junior, C.A. Diaz, L.M. Avellar, M.J. Pontes, C. Marques, A. Frizera, Polymer optical fiber sensors in healthcare applications: A comprehensive review, Sensors 19 (14) (2019) 3156.

[6] Y. Zhao, Y. Jin, J. Wang, X. Dong, Detection of liquid-level variation using a SMS fiber structure, Opt. -Int. J. Light Electron Opt. 124 (18) (2013) 3771–3773.
[7] S.M.A. Musa, A.I. Azmi, A.S. Abdullah, M.Y.M. Noor, R.K.R. Ibrahim, Dual sensing points Mach–Zehnder interferometer for refractive index and discrete liquid level sensing, Optik 241 (2021), 166974.
[8] G. Perrone, A. Vallan, A low-cost optical sensor for noncontact vibration measurements, IEEE Trans. Instrum. Meas. 58 (5) (2008) 1650–1656.
[9] A. Vallan, M.L. Casalicchio, G. Perrone, Displacement and acceleration measurements in vibration tests using a fiber optic sensor, IEEE Trans. Instrum. Meas. 59 (5) (2010) 1389–1396.
[10] S. Grassini, M. Ishtaiwi, M. Parvis, A. Vallan, Design and deployment of low-cost plastic optical fiber sensors for gas monitoring, Sensors 15 (1) (2015) 485–498.
[11] K.I. Suehara, T. Kameoka, A. Hashimoto, Development of simple optical sensor for measurement of sugar content using bent optical fiber, light emitting diode and photo diode, J. Sci. Technol. Light. 41 (2018) 12–21.
[12] Angrasari, F., Arifin, A., & Abdullah, B. (2019, October). Fabrication of Milk Fat Sensor based on Plastic Optical Fiber. In Journal of Physics: Conference Series (Vol. 1341, No. 8, p. 082038). IOP Publishing.
[13] A. Gowri, A.S. Rajamani, B. Ramakrishna, V.V.R. Sai, U-bent plastic optical fiber probes as refractive index based fat sensor for milk quality monitoring, Opt. Fiber Technol. 47 (2019) 15–20.
[14] Bilro, L., Alberto, N., Sá, L.M., Pinto, J.L., & Nogueira, R.N. (2011, July). Side-polished plastic optical fibre as refractive index, cure and viscosity sensor. In International Conference on Applications of Optics and Photonics (Vol. 8001, p. 800142). International Society for Optics and Photonics.
[15] H. Di, Y. Xin, J. Jian, Review of optical fiber sensors for deformation measurement, Optik 168 (2018) 703–713.
[16] W. Zheng, X. Tao, B. Zhu, G. Wang, C. Hui, Fabrication and evaluation of a notched polymer optical fiber fabric strain sensor and its application in human respiration monitoring, Text. Res. J. 84 (17) (2014) 1791–1802.
[17] A. Gowri, V.V.R. Sai, U-bent plastic optical fiber based plasmonic biosensor for nucleic acid detection. In Optical Sensors (May), Int. Soc. Opt. Photonics 10231 (2017), 1023113.
[18] J. Kallweit, M. Pätzel, F. Pursche, J. Jabban, M. Morobeid, T. Gries, An Overview on Methods for Producing Side-Emitting Polymer Optical Fibers, Textiles 1 (2) (2021) 337–360.
[19] F. Francis Berghmans, T. Geernaert, in: L. Thevenaz (Ed.), Chapter 10: Optical Fiber Point Sensors. In Advanced fiber optics, CRC Press, Boca Raton, FL, USA, 2011, pp. 309–344. ISBN 9781315098593.
[20] K.S. Kuang, W.J. Cantwell, P.J. Scully, An evaluation of a novel plastic optical fibre sensor for axial strain and bend measurements, Meas. Sci. Technol. 13 (10) (2002) 1523.
[21] A.G. Leal-Junior, A. Frizera, M.J. Pontes, Sensitive zone parameters and curvature radius evaluation for polymer optical fiber curvature sensors, Opt. Laser Technol. 100 (2018) 272–281.
[22] M.S. Kovacevic, A. Djordjevich, D. Nikezic, Analytical optimization of optical fiber curvature gauges, IEEE Sens. J. 8 (3) (2008) 227–232.
[23] J.B. Wielar, Plastic Optical Fibers. In Fiber Optics Comes of Age III, Int. Soc. Opt. Photonics 31 (1973) 3–12.
[24] A. Djordjevich, M. Boskovic, Curvature gauge, Sens. Actuators A: Phys. 51 (2–3) (1995) 193–198.
[25] A. Djordjevich, Y. He, Thin structure deflection measurement, IEEE Trans. Instrum. Meas. 48 (3) (1999) 705–710.
[26] A. Djordjevich, M. Fung, R.Y. Fung, Principles of deflection-curvature measurement, Meas. Sci. Technol. 12 (11) (2001) 1983.
[27] A. Djordjevich, Alternative to strain measurement, Opt. Eng. 42 (7) (2003) 1888–1892.
[28] Y. Fu, H. Di, R. Liu, Light intensity modulation fiber-optic sensor for curvature measurement, Opt. Laser Technol. 42 (4) (2010) 594–599.
[29] Y. Fu, H. Di, Fiber-optic curvature sensor with optimized sensitive zone, Opt. Laser Technol. 43 (3) (2011) 586–591.
[30] H. Di, Sensing principle of fiber-optic curvature sensor, Opt. Laser Technol. 62 (2014) 44–48.
[31] G. Zhi, H. Di, Wind speed monitoring system based on optical fiber curvature sensor, Opt. Fiber Technol. 62 (2021), 102467.
[32] J. Shen, X. Tao, D. Ying, C. Hui, G. Wang, Light-emitting fabrics integrated with structured polymer optical fibers treated with an infrared CO_2 laser, Text. Res. J. 83 (7) (2013) 730–739.
[33] J. Shen, C. Chui, X. Tao, Luminous fabric devices for wearable low-level light therapy, Biomed. Opt. Express 4 (12) (2013) 2925–2937.
[34] D.Z. Stupar, J.S. Bajic, L.M. Manojlovic, M.P. Slankamenac, A.V. Joza, M.B. Zivanov, Wearable low-cost system for human joint movements monitoring based on fiber-optic curvature sensor, IEEE Sens. J. 12 (12) (2012) 3424–3431.
[35] Z. Gong, Z. Xiang, X. OuYang, J. Zhang, N. Lau, J. Zhou, C.C. Chan, Wearable fiber optic technology based on smart textile: A review, Materials 12 (20) (2019) 3311.
[36] J. Li, J. Liu, C. Li, H. Zhang, Y. Li, Wearable wrist movement monitoring using dual surface-treated plastic optical fibers, Materials 13 (15) (2020) 3291.
[37] C. Teng, S. Deng, H. Deng, H. Yang, Y. Xu, L. Yuan, H. Liu, Investigation of a plastic optical fiber imprinted with V-groove structure for displacement sensing, Opt. Eng. 58 (7) (2019), 072002.
[38] P.S. André, H. Varum, P. Antunes, L. Ferreira, M.G. Sousa, Monitoring of the concrete curing process using plastic optical fibers, Measurement 45 (3) (2012) 556–560.
[39] P. Antunes, J. Dias, T. Paixão, E. Mesquita, H. Varum, P. Andre, Liquid level gauge based in plastic optical fiber, Measurement 66 (2015) 238–243.
[40] E. Mesquita, T. Paixão, P. Antunes, F. Coelho, P. Ferreira, P. Andre, H. Varum, Groundwater level monitoring using a plastic optical fiber, Sens. Actuators A: Phys. 240 (2016) 138–144.
[41] C. Teng, H. Liu, H. Deng, S. Deng, H. Yang, R. Xu, J. Zheng, Liquid level sensor based on a V-Groove structure plastic optical fiber, Sensors 18 (9) (2018) 3111.
[42] H. Bao, B. Wu, Y. Liu, Y. Zhou, J. Zheng, Investigation of long period grating imprinted on a plastic optical fiber for liquid level sensing, Optik 251 (2022), 168367.
[43] P. Xue, F. Yu, B. Wu, H. Bao, J. Zheng, Investigation of a D-shaped plastic optical fiber assisted by a long period grating for refractive index sensing, IEEE Sens. J. 20 (2) (2019) 842–847.
[44] P. Xue, F. Yu, Y. Cao, J. Zheng, Refractive index sensing based on a long period grating imprinted on a multimode plastic optical fiber, IEEE Sens. J. 19 (17) (2019) 7434–7439.
[45] A.W. Snyder, J. Love, Optical Waveguide Theory, Springer Science & Business Media, 2012.
[46] Y.C. Chen, W.F. Xie, Y.L. Ke, L.W. Chen, Power loss characteristics of a sensing element based on a grooved polymer optical fiber under elongation, Meas. Sci. Technol. 19 (10) (2008), 105203.